

1 Automated extraction of local defect resonance using the  
2 principal component analysis in lock-in ultrasonic  
3 vibrothermography

4 Seyed Ali Ghorashi<sup>a</sup>, Farhang Honarvar<sup>a</sup>, Morteza Tabatabaeipour<sup>b,\*</sup>

5 <sup>a</sup>*NDE Lab, Faculty of Mechanical Engineering, K. N. Toosi University of Technology, 7 Pardis St.,  
6 Mollasadra Ave., Vanak Sq., Tehran, Iran*

7 <sup>b</sup>*Centre for Ultrasonic Engineering, Department of Electronic and Electrical Engineering, University of  
8 Strathclyde, Glasgow G11XW, UK*

---

9 **Abstract**

10 Ultrasonic vibrothermography is an emerging and promising nondestructive evaluation tech-  
11 nique used for detection of surface and sub-surface defects. The heat-generating sources such  
12 as friction of the surface asperities of the defect and viscoelastic behavior of the structure  
13 may cause variations in non-linear elastic energy leading to the rise of temperature of the  
14 damaged area. In this paper, a Flat-Bottomed Hole (FBH) defect is modeled by finite el-  
15 ement method in a polymethylmethacrylate (PMMA) structure. The desired information  
16 from this defect is retrieved by its local defect resonance (LDR) frequency which is estimated  
17 through a Principal Component Analysis (PCA). It is shown that the PCA algorithm can  
18 extract the LDR frequency of the FBH with high accuracy. The sample is then excited  
19 by a sine wave at its LDR frequency modulated by a low frequency corresponding to the  
20 thermal penetration depth. The lock-in amplitude and phase images are also generated at  
21 different modulation frequencies in order to find the optimal frequency in terms of contrast  
22 enhancement. The results of the finite element model are then verified by comparison with  
23 published experimental results and are found to be in very good agreement.

24 *Keywords:* Vibrothermography, local defect resonance, principal component analysis

---

\*Corresponding author.

*Email address:* Morteza.Tabatabaeipour@strath.ac.uk (Morteza Tabatabaeipour)

## 25 1. Introduction

26 Ultrasonic vibrothermography is a new nondestructive testing technique introduced in  
27 late 1970s [1]. High test productivity and adaptability to structures with complex geometries  
28 are some of the advantages of this new technique [1]. Recently, the introduction of the local  
29 defect resonance (LDR) has initiated considerable scientific research effort in ultrasonic  
30 vibrothermography [2, 3]. It was also demonstrated that how the LDR, for a circular FBH  
31 defect and delamination, can be extracted by applying an image processing algorithm in  
32 every frequency bin to estimate the position and size of the defect [4]. However, this image  
33 processing algorithm may fail due to an assumption on the round shape of the LDR.

34 Results from earlier studies demonstrate that the heat generation induced by the LDR  
35 leads to high-temperature variation at the defective region [3, 5]. In other words, an external  
36 mechanical energy source causes a temperature difference to be created between the defec-  
37 tive and intact segments of the specimen. This temperature difference makes the defected  
38 region visible to an IR (infrared) camera [6]. The parameters that influence the generation of  
39 heat have been investigated by several researchers and it has been shown that three heating  
40 mechanisms of friction, plasticity, and viscoelasticity are the primary sources of heat gener-  
41 ation [7]. These heat generation mechanisms may act individually or in combination. In the  
42 case of a flat-bottomed hole (FBH) defect, the primary heat source is viscoelasticity, whereas  
43 in delamination and cracks, the combination of both viscoelasticity and friction plays the  
44 main role [8, 9]. Furthermore, a direct relationship between the excitation frequency and  
45 the generated heat on the cracks has been reported by Holland *et al.* [10, 11].

46 Power dissipation at a defect is not the same as its surroundings. This temperature  
47 difference can be measured by using the lock-in principle for each pixel of the surface tem-  
48 perature [12]. In this way, the internal structure of the object can be evaluated by measuring  
49 the amplitudes and phase shifts of surface temperatures with respect to an input reference  
50 signal. The lock-in vibrothermography has been implemented for detection of a variety of  
51 defects including disbonding of ceramic coatings on metallic substrates [13] and a delami-  
52 nation/impact damages in the composite structures [14].

53 The objective of this paper is to evaluate the effectiveness of the Principal Component  
54 Analysis (PCA) algorithm in automatic selection of local defect resonances (LDRs). Fur-  
55 thermore, a search of the literature shows that what we currently know about this new  
56 technique is mostly based on empirical studies. It is rather difficult and expensive to obtain  
57 the optimal parameters by experiment. This paper provides the first numerical study for  
58 the entire process of the LDR-based lock-in vibrothermography. It also paves the way for  
59 further works on the optimization of this inspection process and defect characterization to  
60 be followed in the future.

61 In the first part of this paper, a ceramic piezo actuator mounted on a PMMA structure is  
62 modeled in the COMSOL Multiphysics finite element modeling software package. The piezo  
63 disk is then loaded with a chirp signal spanning a frequency range of 1-200 kHz to extract  
64 the local defect resonance of a flat-bottomed hole (FBH). The out-of-plane component of  
65 the signals is subsequently transformed to the frequency-domain and analyzed by using the  
66 PCA algorithm to extract the local defect resonance (LDR) of the FBH. The PCA results  
67 are then compared with the LDR frequency calculated by an eigenfrequency analysis which  
68 is a stand-alone technique.

69 In the second part of the paper, an amplitude modulated signal with the LDR frequency  
70 as a carrier and a low frequency as the message signal are fed into the ceramic piezo disk.  
71 Then, the lock-in thermography algorithm is applied to the acquired thermal waves to cre-  
72 ate the amplitude and phase images, and finally, the numerical results are compared with  
73 experimental results reported in [2, 3, 15].

#### 74 *1.1. Concept of local defect resonance*

75 If no structural degradation is caused by ultrasonic excitation, the amplitude of ultrasonic  
76 vibrations in a vibrothermography test can be increased to enhance the effectiveness of this  
77 technique. However, this is not always economical or doable due to hardware limitations.  
78 As an alternative approach, exciting the test piece with a Local Defect Resonance (LDR)  
79 frequency, which is the resonance frequency of the local defect, can pump the maximum  
80 amount of energy into the defect region. Therefore, it is good to know the LDR for any type

81 of defect.

82 The local defect resonance can be defined as the natural frequency of the defect with  
83 an effective mass  $m_{eff}$  and effective rigidity  $k_{eff}$  according to the fundamental theory of  
84 vibrations [16, 17]. The following equation can be used for defects with different geometries:

$$f_{LDR} = \frac{1}{2\pi} \sqrt{\frac{k_{eff}}{m_{eff}}} \quad (1)$$

85 For the artificial defect of interest in this paper, which is a circular flat-bottomed hole, the  
86 effective mass and effective rigidity are as follows [16]:

$$m_{eff} = 1.8m, \quad m = \rho\pi R^2 \quad (2)$$

$$k_{eff} = \frac{198\pi D}{R^2} \sqrt{\frac{k_{eff}}{m_{eff}}}, \quad D = \frac{Ed^3}{12(1-\nu^2)} \quad (3)$$

87 where  $D$  is the bending stiffness,  $R$  is the radius of the circular defect,  $d$  is the residual  
88 wall thickness of the FBH,  $E$  is the modulus of elasticity of the specimen,  $\nu$  is the Poisson's  
89 ratio,  $\rho$  is the density and  $m$  is the residual mass of the FBH. By combining equations (1),  
90 (2) and (3), the LDR frequency of a circular FBH is found to be [4, 16]:

$$f_{LDR} = \frac{1}{2\pi} \sqrt{\frac{k_{eff}}{m_{eff}}} \approx \frac{1.6d}{R^2} \sqrt{\frac{E}{12\rho(1-\nu^2)}} \quad (4)$$

## 91 1.2. Thermal analytical approach

92 According to the Fourier's law for a transient heat transfer in a solid with an internal  
93 heat source, the temperature distribution is calculated from the following equation [18]:

$$k_x \frac{\partial^2 T}{\partial x^2} + k_y \frac{\partial^2 T}{\partial y^2} + k_z \frac{\partial^2 T}{\partial z^2} + q = \rho C_p \frac{\partial T}{\partial t} \quad (5)$$

94 where  $T(x,y,z,t)$  is the time-dependent temperature of point  $(x,y,z)$ ,  $k(x,y,z,t)$  is the thermal  
95 conductivity which has identical values along all three coordinate axes due to the isotropic  
96 properties of the sample,  $q$  is the volumetric heat generation in the sample and  $C_p$  is the  
97 specific heat capacity.

98 The boundary condition on the upper surface of the plate, considering convection heat  
 99 transfer, is:

$$-\hat{n} \cdot (-k \nabla T) = h(T_s - T) \quad (6)$$

100 Where  $h=5$  ( $\frac{W}{m^2 K}$ ) is the convective heat transfer coefficient.

101 The generated volumetric heat can be written as [19, 20]:

$$q = \eta \omega W \quad (7)$$

102 In equation (7),  $\eta$  is the structural loss factor,  $\omega$  ( $\frac{rad}{s}$ ) is the angular frequency,  $W$  ( $\frac{J}{m^3}$ ) is  
 103 the elastic strain energy density defined at a specific time as follows [19, 20]:

$$W = \frac{E u_z^2}{2(1 - \nu^2)} \left[ \left( \frac{\partial^2 U}{\partial x^2} \right)^2 + \left( \frac{\partial^2 U}{\partial y^2} \right)^2 + 2\nu \frac{\partial^4 U}{\partial x^2 \partial y^2} + 2(1 - \nu) \left( \frac{\partial^2 U}{\partial x \partial y} \right)^2 \right] \quad (8)$$

104 where  $U = U(x, y, z, t)$  is the displacement which appears due to the harmonic excitation of  
 105 the piezoelectric crystal and  $u_z$  is the out-of-plane component of displacement at the surface  
 106 the of plate.

107 By incorporating equations (7) and (8), the generated heat can be calculated from Eq  
 108 (9) which shows that the induced heat is a quadratic function of the out-of-plane component  
 109 of displacement,  $u_z$ :

$$q = \frac{\eta \omega E u_z^2}{2(1 - \nu^2)} \left[ \left( \frac{\partial^2 U}{\partial x^2} \right)^2 + \left( \frac{\partial^2 U}{\partial y^2} \right)^2 + 2\nu \frac{\partial^4 U}{\partial x^2 \partial y^2} + 2(1 - \nu) \left( \frac{\partial^2 U}{\partial x \partial y} \right)^2 \right] \quad (9)$$

## 110 2. Simulation model setup

111 In order to evaluate the LDR-based vibrothermography, a PMMA sample is modelled in  
 112 COMSOL Multiphysics finite element modeling software package with dimensions of  $200 \times$   
 113  $40 \times 3$  mm<sup>3</sup>, containing an FBH defect with a radius of 10 mm and a depth of 2 mm as shown  
 114 in Fig. 1. The material properties of the sample are given in Table 1. Three different studies  
 115 have been conducted in COMSOL Multiphysics for the analysis of the model as follows:

- 116 • Eigenfrequency analysis: To find the local defect resonance frequency. This is a stand-  
 117 alone analysis, meaning that there is no need for any signal analysis to calculate the  
 118 LDR frequency. The piezo actuator can be disabled during this analysis.

- 119 • Time-domain analysis: To monitor the signals generated by a piezo actuator from  
120 the defect region for Principal Component Analysis (PCA). More details on the wave  
121 propagation and the piezo actuator are given in Section 2.1.
- 122 • Frequency domain analysis coupled with a time-domain study of the heat transfer: To  
123 evaluate the thermal waves generated by a wave-modulated signal in order to plot the  
124 thermosonic images. The frequency-domain study allows us to capture long duration  
125 of signals for numerical analysis. Furthermore, the structural loss factor can only be  
126 applied in the frequency domain analysis module of the software.

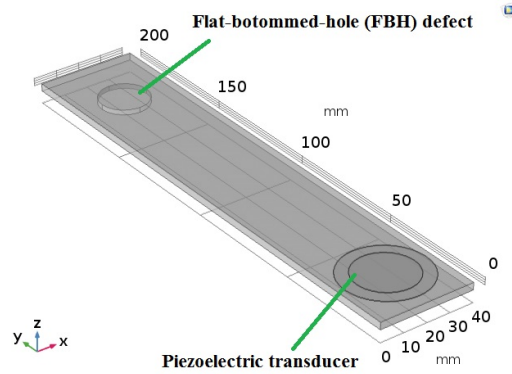


Figure 1: Geometry of the simulated PMMA model, showing the position of both an FBH defect and a piezoelectric actuator.

### 127 2.1. Simulation of wave propagation and the piezo actuator

128 To find the LDR frequency, we use an excitation frequency range of 1-200 kHz. This  
129 range of frequencies can generate several Lamb wave modes in the plate-like structure.  
130 The suitable mesh size is found from the dispersion curves plotted by using the GUIGUW  
131 software [21]. The maximum group velocity in this range is approximately  $2158 \left(\frac{m}{s}\right)$  and the  
132 minimum wavelength is 5.6 mm. To capture the dynamics of ultrasonic vibrations, at least  
133 8 spatial grid points are taken. Furthermore, the Courant-Friedrichs-Lewy (CFL) stability  
134 criterion gives the following strict requirement relationship between the size of elements  $\Delta x$

Table 1: Material properties of the PMMA plate in the FEM analysis

Parameter	Value
Young modulus ( $E$ )	6.18 GPa
Poisson ratio ( $\nu$ )	0.3216
Density ( $\rho$ )	1190 ( $\frac{kg}{m^3}$ )
Thermal conductivity ( $k$ )	0.1905 ( $\frac{W}{m^2 K}$ )
Specific heat capacity ( $C_p$ )	1440 ( $\frac{J}{kg \text{ } ^\circ C}$ )
Thermal diffusivity coefficient ( $\alpha = \frac{k}{\rho C_p}$ )	$1.11 \times 10^{-7}$ ( $\frac{m}{s}$ )
Structural damping coefficient ( $\beta$ )	0.02
Initial temperature ( $T_0$ )	20 $^\circ C$

135 and the time-step size of the solver  $\Delta t$ :

$$\Delta t \leq \frac{\Delta x}{\sqrt{3}C_{max}} \quad (10)$$

136 where  $C_{max}$  is the maximum speed of the ultrasonic waves [22, 23]. A time-step of  $1 \times 10^{-7}$  (s)  
137 is found to be suitable for this model and a tetrahedral mesh was applied to the structure.

138 To verify the model by the experimental data available in the literature [2, 15], the  
139 identical piezo-ceramic actuator (Conrad Electronic GmbH) was used to excite the specimen  
140 in the simulation [2, 24]. As shown in Fig. 2, several resonance peaks are observed in the  
141 frequency range of 1-200 kHz, which depend on the piezo actuator dimensions and its  
142 material properties. Note that the local defect resonance (LDR) is not associated with any  
143 of these piezo resonances. In other words, the resonances of the piezoceramic do not control  
144 the local defect resonance. The specifications of this piezo actuator are listed in Table 2.

145 The out-of-plane signal components from the upper surface ( $z=3$  mm) of the defect region  
146 are monitored for further analysis. The spatial step of 1 mm was chosen for monitoring the  
147 signals in both  $x$  and  $y$  directions.

148

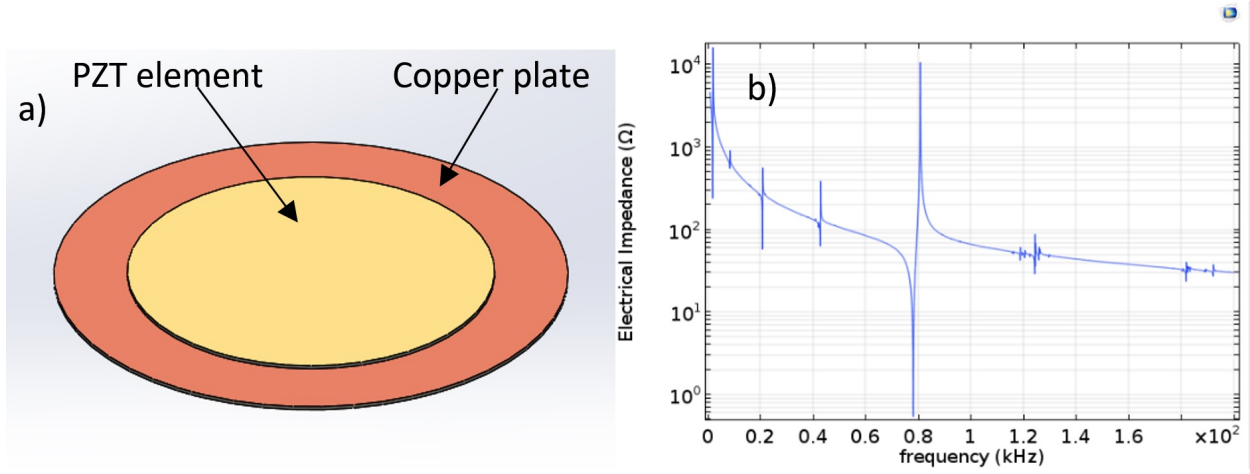


Figure 2: a) The piezo actuator model used in simulations, b) Impedance analysis of the simulated piezo-electric actuator.

Table 2: Piezo actuator specifications exploited in the simulation.

Element diameter (mm)	Plate diameter (mm)	Element thickness (mm)	Plate thickness (mm)	Plate material
25	35	0.26	0.51	Copper

### 149 3. Estimation of Local Defect Resonance (LDR)

#### 150 3.1. Eigenfrequency analysis

151 The LDR of an FBH defect is calculated by using three different approaches which are:  
 152 1) a theoretical equation, 2) eigenfrequency analysis, and 3) Principal Component Analysis  
 153 (PCA). Eigenfrequency analysis is a stand-alone process and for this analysis, we do not  
 154 need to measure any signals for estimating the LDR. Therefore, the LDR obtained from  
 155 eigenfrequency analysis is used as the benchmark.

156 The eigenfrequency analysis does not only provide the local defect resonance but it also  
 157 illustrates the mode-shape. Figure 3 shows the results of eigenfrequency analysis carried out  
 158 in COMSOL Multiphysics at two different frequencies. In Fig. 3a, the excitation frequency  
 159 coincides with one of the resonance frequencies of the whole sample and therefore, the sample  
 160 is seen to be vibrating at its corresponding resonance mode. In Fig. 3b, the excitation

161 frequency coincides with LDR, i.e. 10.47 kHz, and therefore, the amplitude of vibrations at  
 162 the defect region is much higher than the rest of the test sample.

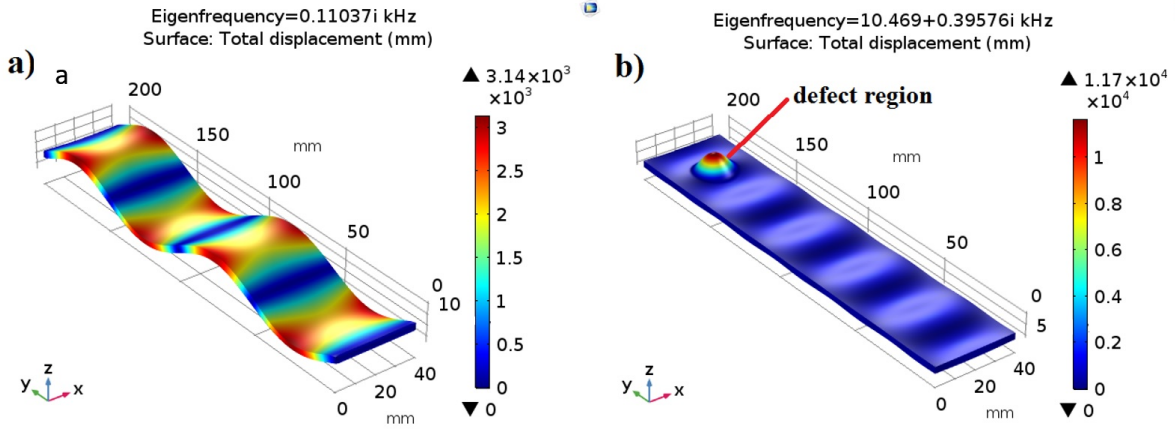


Figure 3: Eigenfrequency analysis performed by using COMSOL Multiphysics at two different frequencies, a) an arbitrary frequency showing one of the resonance modes of the sample, b) at LDR of the FBH defect where large displacements at the defect zone are observed.

162

### 163 3.2. Principal component analysis

164 Principal component analysis (PCA) is a useful technique for analyzing a large dataset  
 165 by increasing its interpretability while minimizing information loss [25, 26]. PCA can be  
 166 described as an N-dimensional ellipsoid matched to the data so that each axis of this ellipsoid  
 167 declares a principal component [26]. The large axes of this ellipsoid, which correspond to  
 168 the maximum variances of the variables, are retained and the small axes with low variances  
 169 are removed. Since LDR produces maximum displacement on top of the defect, it can be  
 170 a powerful tool for extracting the desired information from a 2D array of signals that are  
 171 measured on top of the defect.

172 The out-of-plane displacement components are measured on a  $31 \times 31$  mm<sup>2</sup> region of  
 173 interest on top of the defect region. This gives a data set of 10000 (n)  $\times$  961 (p), where  
 174 n and p represent the number of samples in each measurement and the total number of  
 175 measurements, respectively. This 2D array of time-domain signals is then transformed into  
 176 frequency-domain, resulting in a matrix with similar dimensions. The rows of this matrix

177 correspond to the FFT magnitudes at different frequency bins and the columns correspond  
 178 to different measurements made on the region of interest. The PCA algorithm is then applied  
 179 to this matrix to extract the LDR frequency. In other words, after setting the distribution  
 180 of the data around the origin, the data array is decomposed into three matrices utilizing a  
 181 singular value decomposition (SVD) analysis [25, 26]. Next, by sorting the eigenvalues, an  
 182 eigenvector corresponding to the first or maximum eigenvalue can be described as an axis  
 183 that the most interpretability of data is visible. Figure 4 illustrates the magnitudes of the  
 184 eigenvalues in a descending order which quickly tends to zero. This trend is consistent with  
 185 PCA images as shown in Fig. 5.

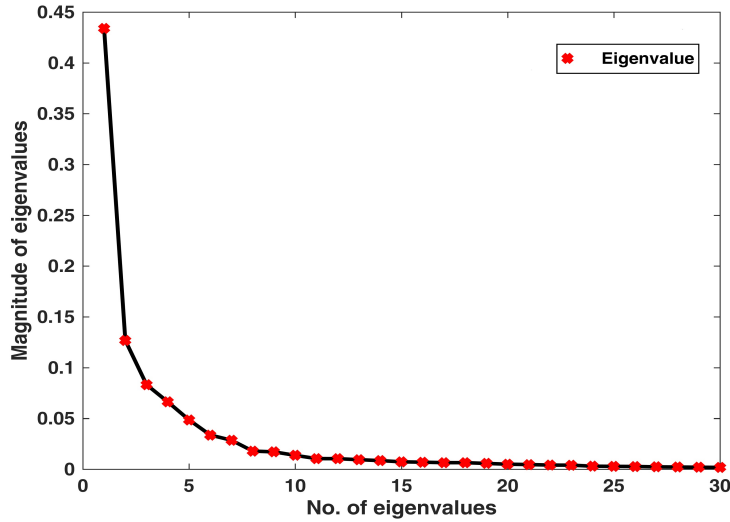


Figure 4: The magnitude of eigenvalues in a descending order showing quick convergence to zero.

186 Figure 6 shows the projection of data onto the first, second, third and fourth axes. Each  
 187 point of this plot represents a frequency bin, allowing us to extract the LDR frequency by  
 188 finding the higher values of the principal components. By extracting the matrix of features  
 189 around the second principal component, the LDR frequency of the FBH is found to be 10.4  
 190 kHz. It is important to note that the LDR frequency of the FBH defect can only be depicted  
 191 (without any other distracting frequency components) on the second principal eigenvalue  
 192 (see Fig. 6). In other words, the image obtained from the second principal component only  
 193 contains the LDR frequency of the FBH. The matrix of features extracted from the first

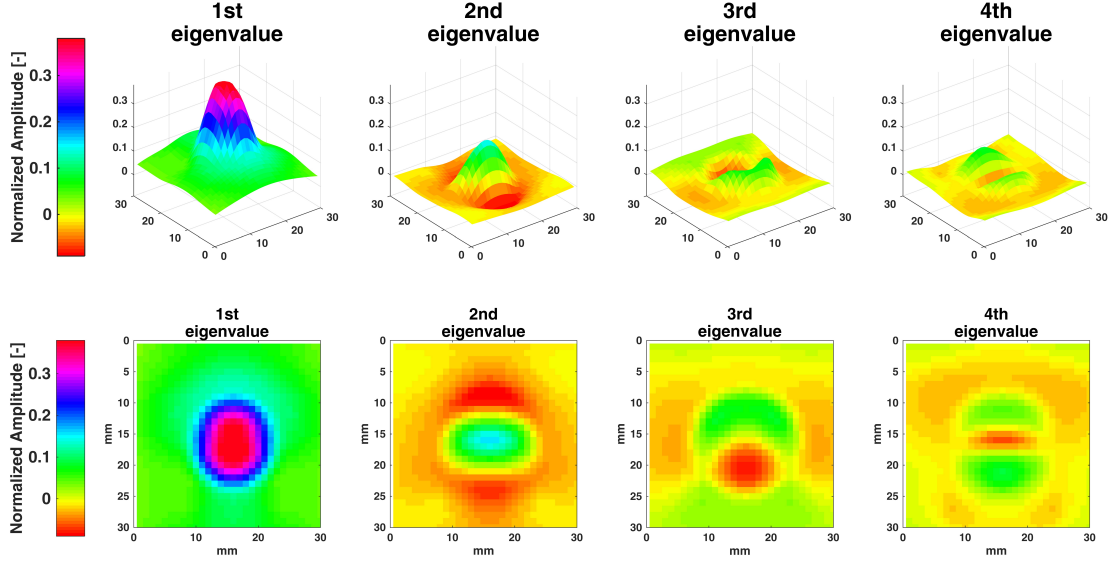


Figure 5: PCA images of different modes showing the consistency of the eigenvectors with the results reported in Fig. 4.

194 principal eigenvalue (see Figs. 5 and 6) includes additional frequencies in addition to the  
 195 LDR frequency, which are due to the resonance frequencies of the sample (e.g. at 3.5 kHz)  
 196 and the higher harmonics of the FBH defect (e.g. at 17.8 kHz).

### 197 3.3. A comparison between local defect resonances

198 In this section, the calculated and the experimental LDR frequencies reported in [2, 15]  
 199 are compared with the calculated LDR frequency through an eigenfrequency analysis. The  
 200 relative error is calculated by equation (11) and is reported in Table 4.

$$error = \frac{|f_{LDR,eigenfrequency} - f_{LDR,i}|}{f_{LDR,eigenfrequency}} \quad i = 1, 2, 3 \quad (11)$$

201 where  $f_{LDR,i}$ ,  $i = 1, 2, 3$  are the LDR frequencies obtained by theory, PCA algorithm and  
 202 experiment, respectively. Note that the experimental LDR frequency given in [2, 15] is 11  
 203 kHz. This comparison confirms that PCA analysis of the monitored signals can extract the  
 204 local defect resonance (LDR) frequency with little error.

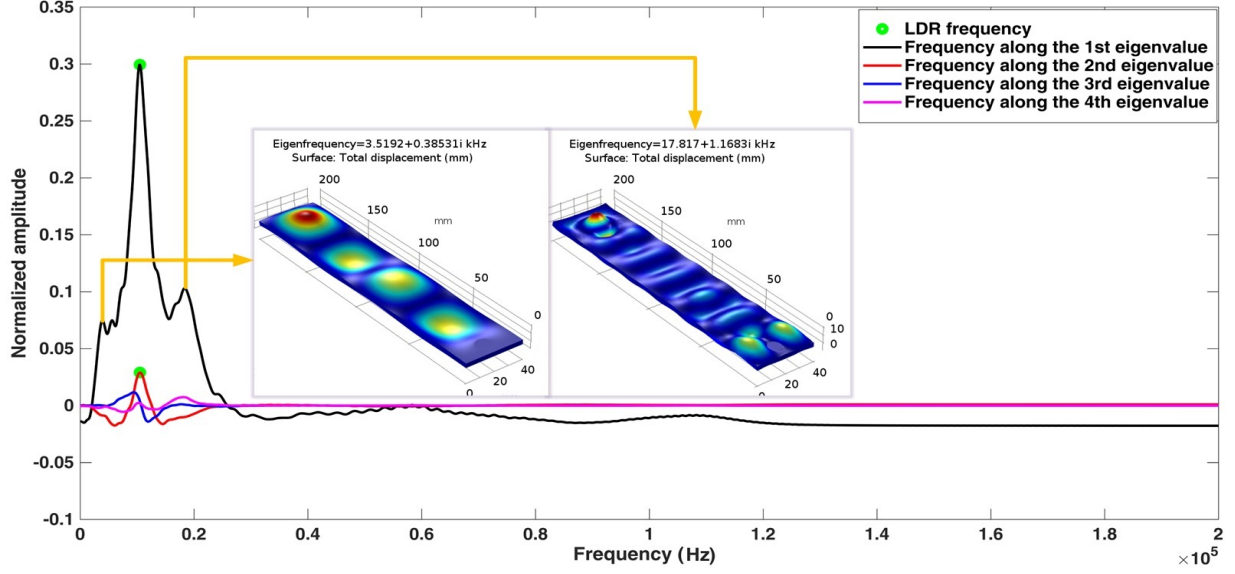


Figure 6: A comparison between the first, second, third and fourth principal axes which shows that only the 1st and 2nd principal components depict the LDR frequency of the FBH defect at 10.4 kHz. Note that the 2nd principal component has a lower amplitude compared to the 1st mode. In contrast, the 2nd mode only provides the LDR peak whereas the 1st mode gives rise to multiple local peaks corresponding to higher resonance frequencies of FBH defect and/or the sample resonances in addition to LDR frequency.

Table 3: Comparison of LDR frequencies obtained from theory, PCA algorithm and experiment.

Method	Source	LDR frequency [kHz]	Error [%]
Theoretical equations	Eq. 4	11.12	6.21
PCA algorithm	Fig. 6	10.4	0.67
Experimental analysis	[2, 15]	11	5.06

## 205 4. Thermal patterns via lock-in algorithm

### 206 4.1. Thermal penetration depth

207 To investigate the thermal images, the sample is excited by a sinusoidal frequency which  
 208 combines a modulated carrier signal  $U_c(t)$ :

$$U_c(t) = u_1 \sin(2\pi f_1 t + \phi_1) \quad (12)$$

209 with a message signal  $U_m(t)$ ;

$$U_m = u_2 \sin(2\pi f_2 t + \phi_2) \quad (13)$$

210 where  $u_1$  and  $u_2$  are the amplitudes of two sine signals. The LDR frequency,  $f_1$ , is carried by  
 211 a lower frequency signal,  $f_2$ , which is related to the thermal diffusion length  $\mu$ . This thermal  
 212 diffusion length,  $\mu$ , is a decay rate of thermal waves which is correlated to the depth of the  
 213 defect,  $Z$ , as follows [27, 28]:

$$Z = C \sqrt{\frac{\alpha}{\pi f_2}} = C\mu, \quad \alpha = \frac{k}{\rho C_p} \quad (14)$$

214 where  $C$  is a correlation constant and  $\alpha$  is the thermal diffusivity. The values of  $C=1$  and  
 215  $1.5 < C < 2$  are usually used for calculation of amplitude and phase, respectively [27, 28].  
 216 These images can be constructed by a lock-in algorithm which will be discussed in more  
 217 detail in section 4.2. Table 4 presents the calculated diffusion lengths and the blind fre-  
 218 quencies for both amplitude and phase images based on the depth of the defect.

219 There is no sufficient phase contrast for defect detection at frequencies higher than the  
 220 limiting frequency  $f_2$ , also known as the blind frequency [27]. By substituting Eq (17) into  
 221 Eq (5), the thermal distribution pattern will turn out to be:

222

$$\frac{\partial^2 T}{\partial x^2} + \frac{\partial^2 T}{\partial y^2} + \frac{\partial^2 T}{\partial z^2} + \frac{q}{k} = \frac{1}{\alpha} \frac{\partial T}{\partial t} \quad (15)$$

Table 4: Theoretically calculated thermal diffusion length and the blind frequency for the FBH defect.

Amplitude Image		Phase Image	
Diffusion length (mm)	Frequency (Hz)	Diffusion length (mm)	Frequency (Hz)
2	0.009	1.11	0.03

223 Numerous studies have indicated that the phase is less sensitive than the amplitude  
 224 to reflections originating from the surrounding area, non-uniform heating, and the surface  
 225 emissivity variations [27].

226 The high frequency (LDR frequency) acts as a carrier delivering heating energy into the  
 227 specimen and the blind frequency produces the desired thermal wave length.

228

229 *4.2. Thermal wave processing by using the lock-in algorithm*

230 The lock-in procedure is now applied to the thermal waves on the surface of the specimen.  
 231 The lock-in thermography takes advantage of sine/cosine correlations. The weighting factors  
 232 of the in-phase and quadrature components of the correlated signals are measured by the  
 233 sine and cosine functions, respectively [12]. These two components of each surface pixel are  
 234 then used to generate the phase and amplitude images as shown in Fig. 7. It is important to  
 235 note that to construct the phase and amplitude images, at least four frames per modulation  
 236 frequency is required [12, 29, 30]. Therefore, a frame rate of 50 Hz is selected for the thermal  
 237 wave acquisition.

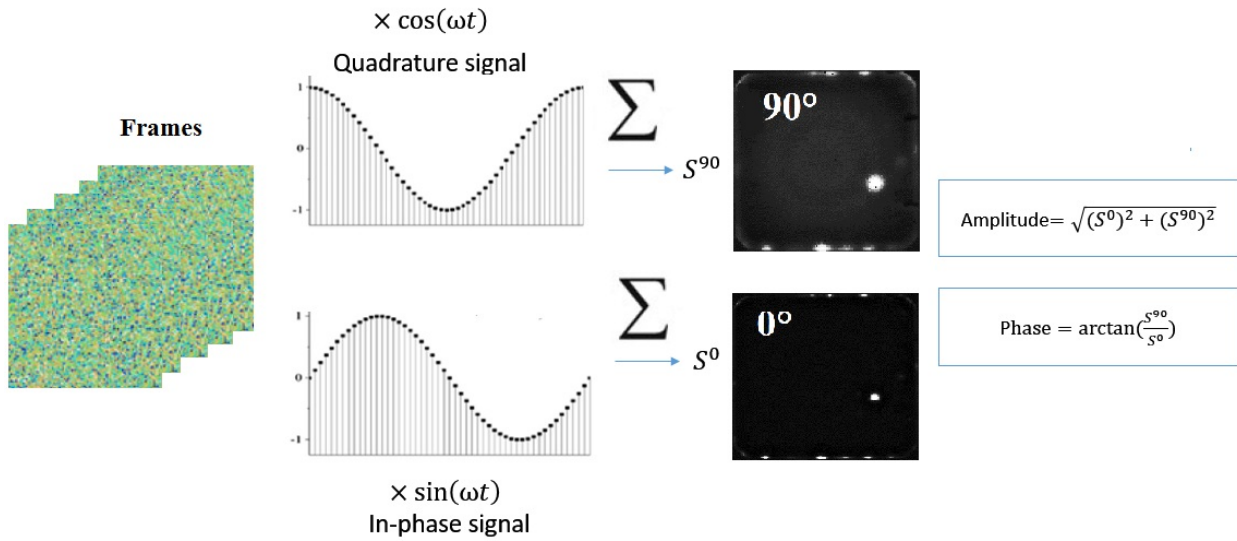


Figure 7: Schematic of the lock-in process applied to the frames obtained by an IR camera.

238 Theoretical modulation frequencies are given in Table 4. However, in order to analyze the  
 239 role of the modulation frequency on the phase and amplitude images, a range of modulation  
 240 frequencies from 0.009 Hz to 0.035 Hz, corresponding to  $C=1$  to 2, is considered. To quantify

241 the result, a signal-to-noise ratio (SNR) is calculated for each amplitude and phase image  
 242 by using the following equations [31]:

$$SNR(Am) = \frac{|\overline{Am_D} - \overline{Am_N}|}{\sigma(Am_N)} \quad (16)$$

$$SNR(Ph) = \frac{|\overline{Ph_D} - \overline{Ph_N}|}{\sigma(Ph_N)} \quad (17)$$

243 where  $\overline{Am_D}$  and  $\overline{Ph_D}$  are respectively the mean values of amplitude and phase in a defective  
 244 region,  $\overline{Am_N}$  and  $\overline{Ph_N}$  are respectively the mean values of the amplitude and phase in a non-  
 245 defective region,  $\sigma(Am_N)$  and  $\sigma(Ph_N)$  are respectively the standard deviation of amplitude  
 246 and phase in a non-defective region, respectively.

247 The SNR results show that the maximum SNR in amplitude and phase images occurs  
 248 at 0.009 Hz and 0.02 Hz, respectively, as shown in Figs. 8 and 9. The value of the parameter  
 249  $C$ , defined by Eq. 14, is given next to each marker used for plotting Figs. 8 and 9. Im-  
 250 ages obtained by the lock-in algorithm and SNR graphs show that the maximum contrast  
 251 in amplitude and phase is achieved at modulation frequencies of 0.009 Hz and 0.02 Hz,  
 252 respectively.

253 To get more insight into this analysis, Fig. 10 illustrates a typical example of the phase  
 254 and amplitude images at the optimal and the extreme limits of the frequency range. Figure  
 255 10 shows that the minimum and maximum temperature amplitudes occur at 0.03 Hz and at  
 256 0.009 Hz, respectively, whereas the minimum and maximum phase contrasts are observed  
 257 at 0.009 Hz and at 0.02 Hz, respectively.

258 To further measure the damaged area, the Otsu's thresholding (*graythresh*) [4, 32] was  
 259 applied to both the phase and amplitude images obtained by the lock-in algorithm. Fig. 11  
 260 shows a typical example of this thresholding process on amplitude and phase images at 0.02  
 261 Hz. The relative errors compared to the real value of the defective area (314.16) are then  
 262 listed in Table 5.

263 The results confirm that the phase images can estimate the damaged area much better  
 264 than the amplitude images, see Table 5. Results obtained by combining the lock-in algo-  
 265 rithm, SNR analysis and the Otsu's thresholding show that the 0.02 Hz frequency is the

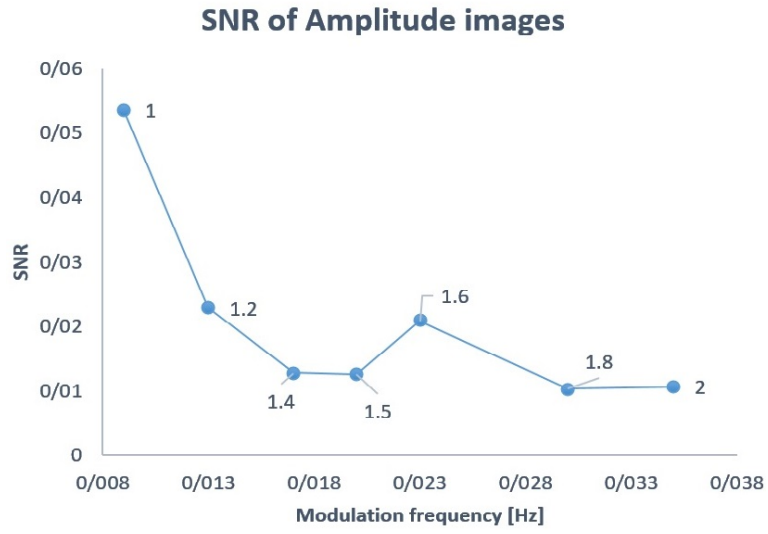


Figure 8: SNR of amplitude images as a function of modulation frequency showing that the maximum SNR occurs at 0.009 Hz.

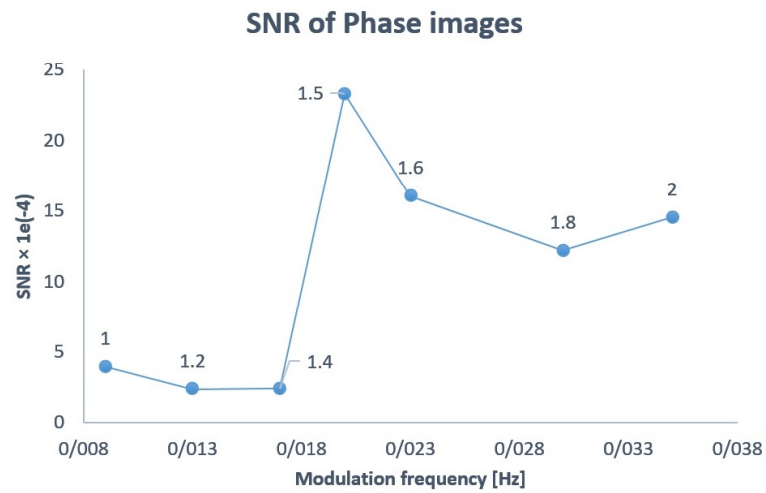


Figure 9: SNR of phase images as a function of modulation frequency showing that the maximum SNR occurs at 0.02 Hz.

266 optimal modulation frequency when the value of  $C$  is set to 1.5. Note that, this frequency  
 267 has also been used as a modulation frequency in the experimental analysis conducted in [15].

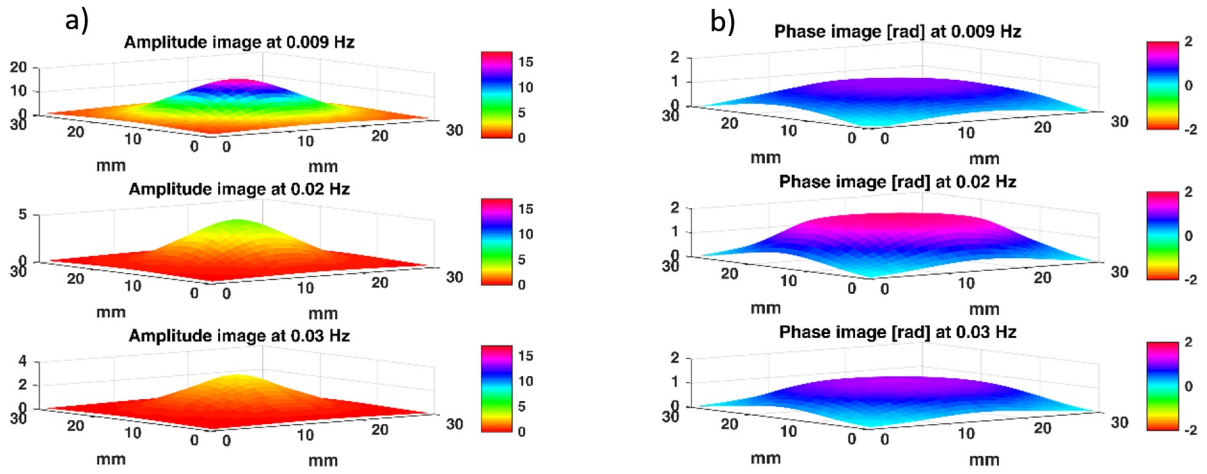


Figure 10: A typical example of amplitude and phase images obtained by the lock-in algorithm at the modulation frequency of 0.009 Hz, 0.02 Hz, and 0.03 Hz, a) Amplitude images, b) Phase images.

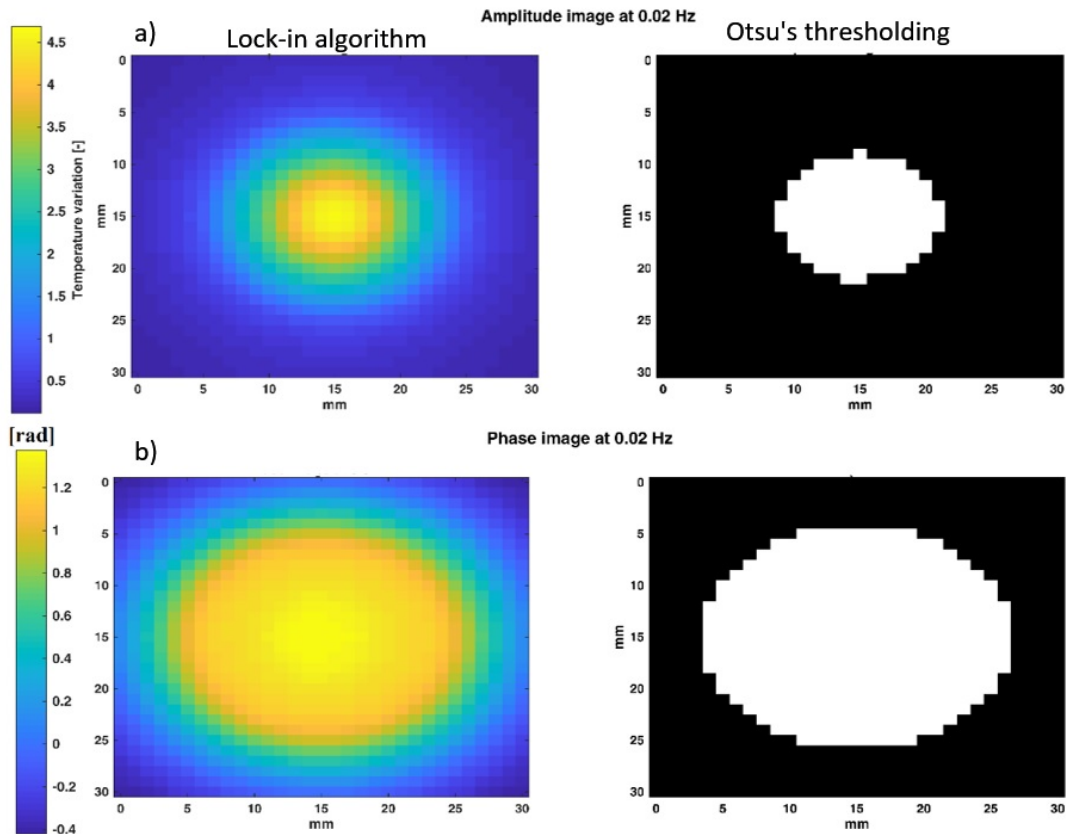


Figure 11: Typical images obtained by lock-in algorithm and Otsu's thresholding at 0.02 Hz, a) Amplitude, b) Phase, showing that the phase images are more accurate in estimating the size of defect.

Table 5: Calculated defective area for the FBH defect based on the Otsu's thresholding shown in Fig.11.

Modulation frequency [Hz]	Amplitude images (mm <sup>2</sup> )	Error [%]	Phase Images (mm <sup>2</sup> )	Error [%]
0.009	120.39	61.7	396.51	26.2
0.02	108.51	65.5	359.9	14.5
0.03	100.28	68.1	394.91	25.7

### 268 4.3. Verification

269 In this Section, we will verify the numerical results obtained for the thermal pattern and  
 270 temperature variations by comparing them with the experimental results reported in the  
 271 literature [2, 3, 15].

272 Figure 12 compares the experimental and simulated results of temperature variations  
 273 of the specimen as a function of the input voltage. As the driving voltage increases, the  
 274 vibration amplitude and the elastic strain energy density in the defect (FBH) area also  
 275 increases. A quadratic dependence between the input voltage and the temperature variation  
 276 is also observed, see Eqs. (8) and (9).

277 Moreover, Fig. 13 illustrates the simulated temperature variations of the defect area at  
 278 30 V input voltage with one modulation cycle of 0.02 Hz. The temperature variation of 380  
 279 mK at the time instant of 50 s is in good agreement with the temperature variations shown  
 280 in Fig. 12 at 30 V. It is evident that the temperature variations decline towards the initial  
 281 temperature value when the excitation is stopped at 50 s.

282 In Fig. 14, the thermal patterns measured on the surface of the specimen around the  
 283 flat-bottomed hole are plotted by using the FEM and experimental results [2, 3]. It can  
 284 be observed that the FEM thermosonic images are in good agreement with experimental  
 285 results reported in [3]. The additional white ring observed in the experimental thermosonic  
 286 image of the FBH is due to a shallow step formed around the FBH during the manufacturing  
 287 process [3].

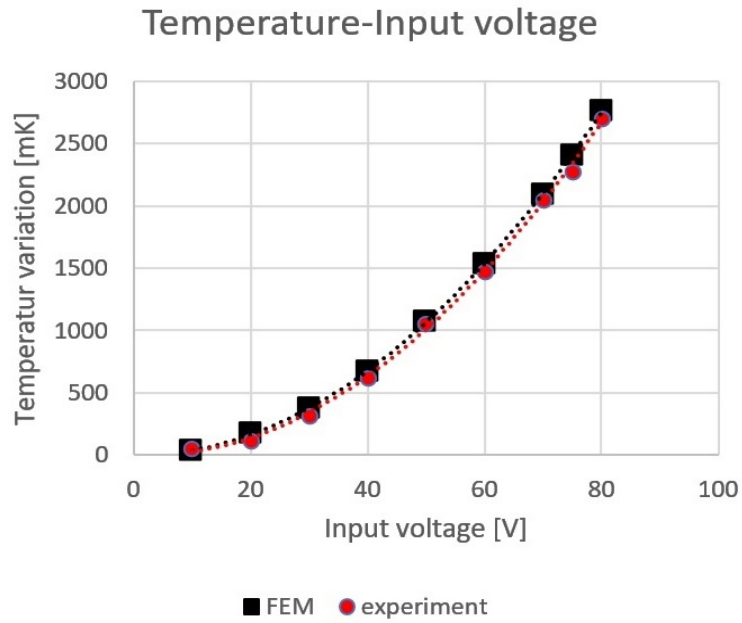


Figure 12: A Comparison of temperature variations as a function of input voltage between FEM and experimental data reported in [15] shows good agreement between the numerical and experimental data.

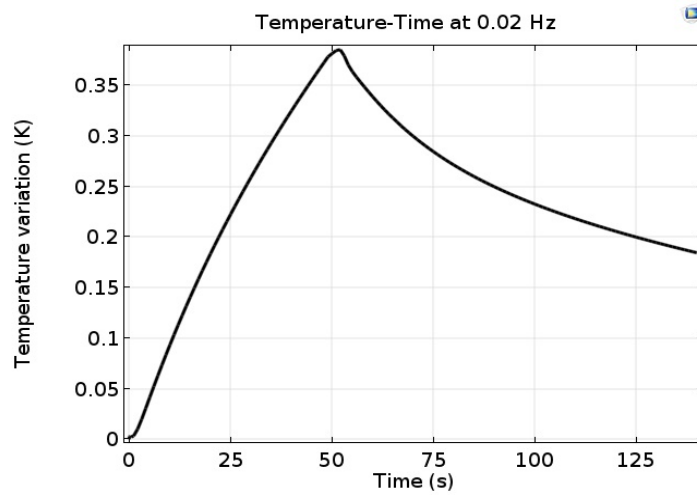


Figure 13: Temperature variation of FBH at LDR frequency with 30 V input voltage, showing that the maximum temperature variation during one modulation cycle is about 0.38K. This is in a good agreement with the temperature variations of Fig.12 at 30V input.

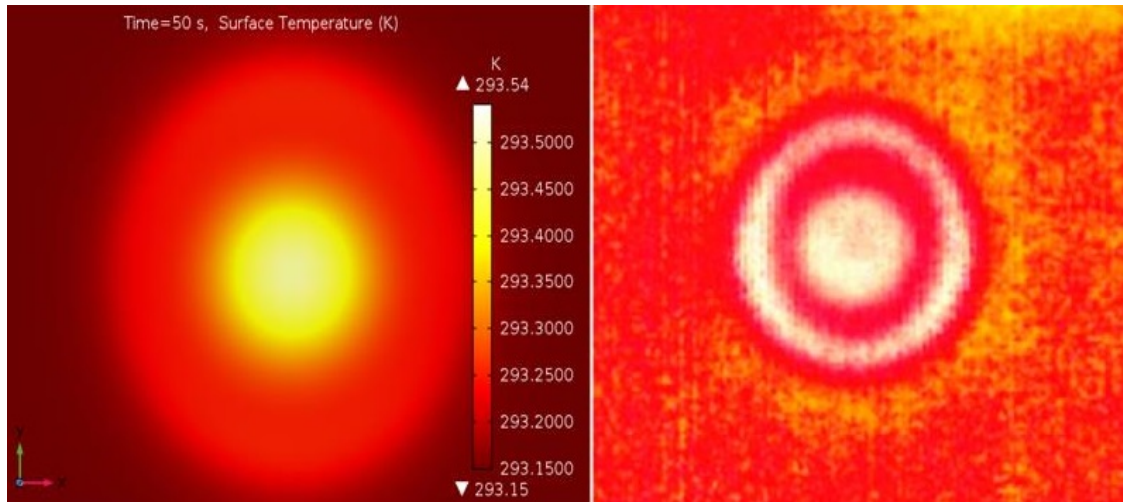


Figure 14: Thermal patterns at the defect area (FBH), a) FEM results, b) experimental results [2, 3]. Note that an extra ring has emerged in the experimental thermosonic image due to the “stretching” of the FBH defect near to its boundary.

## 288 5. Conclusion

289 In this paper, a PMMA plate structure containing a flat-bottomed-hole (FBH) was sim-  
 290 ulated by finite element method in COMSOL Multiphysics software package. The plate was  
 291 excited by a chirp signal through a piezo-ceramic actuator mounted on the structure. The  
 292 out-of-plane components of the top surface displacement signal were then used to measure  
 293 the local defect resonance (LDR) frequency of the FBH through a principal component  
 294 analysis algorithm. The LDR frequencies obtained from the theoretical equations, PCA  
 295 algorithm, and the published experimental results in [2, 15] were compared with the cal-  
 296 culated LDR through an eigenfrequency analysis. The results confirm that the Principal  
 297 Component Analysis (PCA) can accurately estimate the LDR frequency.

298 Thermal diffusion length, which corresponds to the modulation frequency, was found to  
 299 be an essential parameter in the study of phase and amplitude of thermal waves. To construct  
 300 the phase and amplitude images, the lock-in algorithm was applied to thermal waves. The  
 301 thermal pattern at the defect area and the effect of the input voltage on the temperature  
 302 were validated by comparison with the experimental data available in the literature [2, 3, 15].

303 The results confirmed a quadratic dependence between the driving voltage and temperature  
304 variations. Furthermore, the optimal modulation frequency was found by quantifying the  
305 amplitude and phase images and estimating the defect size.

306 Future research is expected to explore the identification and sizing of other defect types  
307 such as cracks, porosity and delamination. Moreover, the effect of material properties such  
308 as anisotropy and homogeneity as observed in composite and multilayered materials on  
309 vibrothermography testing is also interesting topics that should be investigated.

## 310 References

- 311 [1] X. Guo, An analytical model and parametric analysis of ultrasound-excited infrared thermography,  
312 Quantitative InfraRed Thermography Journal 12 (2015) 137–148.
- 313 [2] I. Solodov, M. Rahammer, D. Derusova, G. Busse, Highly-efficient and noncontact vibro-thermography  
314 via local defect resonance, Quantitative InfraRed Thermography Journal 12 (2015) 98–111.
- 315 [3] I. Solodov, D. Derusova, M. Rahammer, Thermosonic chladni figures for defect-selective imaging,  
316 Ultrasonics 60 (2015) 1–5.
- 317 [4] J. Hettler, M. Tabatabaeipour, S. Delrue, K. Van Den Abeele, Detection and characterization of  
318 local defect resonances arising from delaminations and flat bottom holes, Journal of Nondestructive  
319 Evaluation 36 (2017) 2.
- 320 [5] T. Zweschper, A. Dillenz, G. Riegert, D. Scherling, G. Busse, Ultrasound excited thermography using  
321 frequency modulated elastic waves, Insight-Non-Destructive Testing and Condition Monitoring 45  
322 (2003) 178–182.
- 323 [6] S. M. Parvasi, C. Xu, Q. Kong, G. Song, Detection of multiple thin surface cracks using vibrothermog-  
324 raphy with low-power piezoceramic-based ultrasonic actuator—A numerical study with experimental  
325 verification, Smart Materials and Structures 25 (2016) 055042.
- 326 [7] X. Han, M. Sarwar Islam, G. Newaz, L. Favro, R. Thomas, Finite element modeling of the heating of  
327 cracks during sonic infrared imaging, Journal of applied physics 99 (2006) 074905.
- 328 [8] R. Montanini, F. Freni, Investigation of heat generation sources in sonic infrared thermography using  
329 laser doppler vibrometry, Proceedings of Quantitative Infrared Thermography QIRT (2012).
- 330 [9] J. Renshaw, J. C. Chen, S. D. Holland, R. B. Thompson, The sources of heat generation in vibrother-  
331 mography, NDT & E International 44 (2011) 736–739.
- 332 [10] S. D. Holland, C. Uhl, Z. Ouyang, T. Bantel, M. Li, W. Q. Meeker, J. Lively, L. Brasche, D. Eisenmann,  
333 Quantifying the vibrothermographic effect, NDT & E International 44 (2011) 775–782.

- 334 [11] S. D. Holland, C. Uhl, J. Renshaw, Toward a viable strategy for estimating vibrothermographic  
335 probability of detection, in: AIP Conference Proceedings, volume 975, AIP, 2008, pp. 491–497.
- 336 [12] O. Breitenstein, W. Warta, M. C. Schubert, M. Langenkamp, Lock-in thermography: Basics and use  
337 for evaluating electronic devices and materials, volume 10, Springer, 2018.
- 338 [13] A. Gleiter, G. Riegert, T. Zweschper, G. Busse, et al., Ultrasound lock-in thermography for advanced  
339 depth resolved defect selective imaging, *Insight-Non-Destructive Testing and Condition Monitoring* 49  
340 (2007) 272.
- 341 [14] A. Salazar, A. Mendioroz, E. Apiñaniz, A. Oleaga, P. Venegas, I. Sáez-Ocáriz, Characterization of  
342 delaminations by lock-in vibrothermography, in: *Journal of Physics: Conference Series*, volume 214,  
343 IOP Publishing, 2010, p. 012079.
- 344 [15] I. Solodov, Local defect resonance (ldr): A route to highly efficient thermosonic and nonlinear ultrasonic  
345 ndt, in: AIP Conference Proceedings, volume 1581, AIP, 2014, pp. 1663–1670.
- 346 [16] I. Solodov, J. Bai, G. Busse, Resonant ultrasound spectroscopy of defects: case study of flat-bottomed  
347 holes, *Journal of Applied Physics* 113 (2013) 223512.
- 348 [17] W. Thomson, M. Dahleh, Theory of vibration with applications, 1993, New Jersey: A Simon &  
349 Schuster Company (1993).
- 350 [18] J. P. Holman, Heat transfer (mcgraw-hill series in mechanical engineering), 2010.
- 351 [19] X. Guo, L. Zhu, 14th quantitative infrared thermography conference, volume 47, Germany, 2018, pp.  
352 178–184.
- 353 [20] J. K. Miller, D. C. Woods, J. F. Rhoads, Thermal and mechanical response of particulate composite  
354 plates under inertial excitation, *Journal of Applied Physics* 116 (2014) 244904.
- 355 [21] [www.guiguw.com](http://www.guiguw.com)
- 356 [22] P. Fellingner, R. Marklein, K. Langenberg, S. Klaholz, Numerical modeling of elastic wave propagation  
357 and scattering with elastodynamic finite integration technique, *Wave motion* 21 (1995) 47–66.
- 358 [23] C. A. Leckey, K. R. Wheeler, V. N. Hafiychuk, H. Hafiychuk, D. A. Timuçin, Simulation of guided-  
359 wave ultrasound propagation in composite laminates: Benchmark comparisons of numerical codes and  
360 experiment, *Ultrasonics* 84 (2018) 187–200.
- 361 [24] [www.produktinfo.conrad.com](http://www.produktinfo.conrad.com)
- 362 [25] A. Ilin, T. Raiko, Practical approaches to principal component analysis in the presence of missing  
363 values, *Journal of Machine Learning Research* 11 (2010) 1957–2000.
- 364 [26] I. T. Jolliffe, J. Cadima, Principal component analysis: a review and recent developments, *Philosophical  
365 Transactions of the Royal Society A: Mathematical, Physical and Engineering Sciences* 374 (2016)  
366 20150202.
- 367 [27] C. Ibarra Castanedo, Quantitative subsurface defect evaluation by pulsed phase thermography: depth

- 368 retrieval with the phase (2005).
- 369 [28] S. Ranjit, K. Kang, W. Kim, Investigation of lock-in infrared thermography for evaluation of subsurface  
370 defects size and depth, *International Journal of Precision Engineering and Manufacturing* 16 (2015)  
371 2255–2264.
- 372 [29] O. Breitenstein, J. Rakotoniaina, F. Altmann, T. Riediger, M. Gradhand, New developments in ir  
373 lock-in thermography, in: *Proc. 30th ISTFA, 2004*, pp. 595–599.
- 374 [30] N. Tabatabaei, Development of Frequency and Phase Modulated Thermal-wave Methodologies for  
375 Materials Non-destructive Evaluation and Thermophotonic Imaging of Turbid Media, Ph.D. thesis,  
376 2012.
- 377 [31] J. Liu, W. Yang, J. Dai, Research on thermal wave processing of lock-in thermography based on  
378 analyzing image sequences for ndt, *Infrared Physics & Technology* 53 (2010) 348–357.
- 379 [32] N. Otsu, A threshold selection method from gray-level histograms, *IEEE transactions on systems,  
380 man, and cybernetics* 9 (1979) 62–66.